International Journal of Minerals, Metallurgy and Materials
Volume 29, Number 9, September 2022, Page 1683
https://doi.org/10.1007/s12613-022-2439-y

Invited Review

Review of electrodeposition methods for the preparation of high-entropy alloys

Zahra Shojaei✉, *Gholam Reza Khayati*, *and Esmaeel Darezereshki*

Department of Materials Science and Engineering, Shahid Bahonar University of Kerman, Kerman 76135-133, Iran
(Received: 16 November 2021; revised: 11 February 2022; accepted: 14 February 2022)

Abstract: High-entropy alloys (HEAs) are suitable for engineering applications requiring excellent mechanical, corrosion, thermal, and magnetic properties. In the last decade, electrodeposition has emerged as a promising synthesis technique for HEAs. Research has focused on the influence of procedure parameters on the deposition of different HEA layers and the effect of their microstructure on their corrosion and magnetic properties. This review of current literature provides comprehensive information on HEAs and the use of direct and pulse electrodeposition as a synthesis technique for these materials. This review also addresses the research gaps on HEA production via electrodeposition, such as using other ceramic particles instead of graphene oxide in composite structures based on HEAs.

Keywords: high-entropy alloy; electrodeposition; corrosion resistance; magnetic properties

1. Introduction

Since 1970, various materials have been developed for different applications. Alloy systems consist mainly of one element and are added with other materials in small quantities. Examples of these traditional alloys include ferrous and non-ferrous alloys such as steels, bronzes, aluminum, and magnesium alloys. A new class of alloys called high-entropy alloys (HEAs) was recently explored to achieve the desired alloy properties [1–2]. These solid-solution alloys consist of five basic elements with equal atomic ratios or 5at%–35at%. Although these alloys have a simple structure with minimal complexity, they have a high mixing entropy that decreases the free energy of their structure. The high configurational entropy in these alloys also provides them with better mechanical, corrosion, thermal, tribological (wear, friction, and lubrication), damping, irradiation, and magnetic properties than conventional alloys. HEAs have vast applications in the nuclear industry, chemical plants, marine applications, aerospace, and gas turbine [1–4]. The following methods can be used to produce these alloys:

(i) Liquid phase route such as arc and induction melting, laser melting, electric resistance melting, thermal spray, and laser cladding [5–10];

(ii) Gas-phase methods such as molecular beam epitaxy, vapor deposition, magnetron sputtering, pulsed laser deposition, and atomic layer deposition [11–14];

(iii) Solid-phase techniques such as mechanical alloying [15–20];

(iv) Chemical process such as sol–gel [21];

(v) Electrochemical synthesis such as electrodeposition [22–34].

Among these techniques, electrodeposition is the newest and has received great attention because of its cost-effectiveness, availability of its raw materials, less equipment intensiveness, and less complexity. In this process, various coating properties can be achieved by changing the current density, applied potential, and bath conditions [35–36]. The first study on HEA electroplating was reported by Yao *et al*. [22] in 2008. Since then, this method has been further developed to produce HEAs, and several reports have been published in this field, as shown in Fig. 1. Although a number of review articles have been published on HEA production, none have focused on electrodeposition. In the present study, all research works on HEA electroplating were reviewed.

2. Thermodynamics of HEAs

The most important thermodynamic quantity in HEAs is the mixing entropy (ΔS_{mix}) [37], which is composed of four types, namely, configuration entropy ($\Delta S_{\text{mix}}^{\text{conf}}$), vibration entropy ($\Delta S_{\text{mix}}^{\text{vib}}$), magnetic dipole entropy ($\Delta S_{\text{mix}}^{\text{mag}}$), and electronic randomness entropy ($\Delta S_{\text{mix}}^{\text{elec}}$), and is calculated using Eq. (1):

$$\Delta S_{\text{mix}} = \Delta S_{\text{mix}}^{\text{conf}} + \Delta S_{\text{mix}}^{\text{vib}} + \Delta S_{\text{mix}}^{\text{mag}} + \Delta S_{\text{mix}}^{\text{elec}} \quad (1)$$

Except for configuration entropy, the other three types of entropy are usually negligible. Hence, the mixing entropy is considered equal to the configuration entropy. For an ideal random component solid solution, the configurational entropy per mole is defined as Eq. (2) [38]:

$$\Delta S_{\text{mix}} = \Delta S_{\text{mix}}^{\text{conf}} = -R\sum_{i=1}^{n} c_i \ln c_i \quad (2)$$

where c_i, R, and n are mole fractions of ith element, gas con-

✉ Corresponding author: Zahra Shojaei E-mail: zahra.shojaei.me@gmail.com

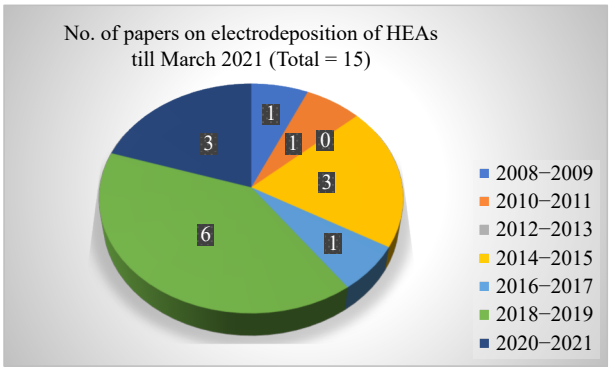

Fig. 1. Number of published papers about the preparation of HEAs by electrodeposition.

stant, and the number of components, respectively [39]. On the basis of the above relation, the alloys are divided into three categories as shown in Fig. 2.

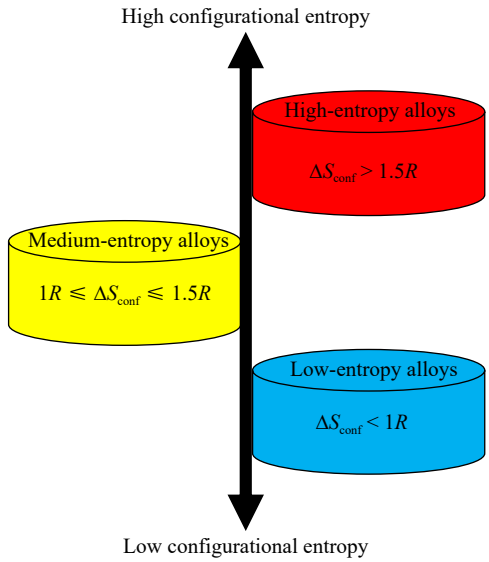

Fig. 2. Classification of alloys based on configurational entropy.

3. Core effects of HEAs

HEAs have the following core effects [40]: high-entropy effect, sluggish diffusion effect, severe lattice distortion, and cocktail effect.

3.1. High-entropy effect

For HEAs, the number of formed phases does not correspond to the ones predicted using the Gibbs phase rule because their mixing entropy creates a solid solution instead of intermetallic compounds [41]. For example, in the $Al_xCoCrFeNiTi_y$ system (with six components) at constant pressure, the Gibbs phase rule predicts seven equilibrium phases at an invariant reaction. By contrast, research showed that even with a change in the percentage of aluminum and titanium, a maximum of four phases are formed in this alloy [42].

In addition, according to Eq. (3):

$$\Delta G_{mix} = \Delta H_{mix} - T\Delta S_{mix} \quad (3)$$

where ΔG_{mix} is the Gibbs free energy change, ΔH_{mix} is the enthalpy change, ΔS_{mix} is the entropy change, and T is the absolute temperature. Increasing the mixing entropy in a HEA system will decrease the free energy of the structure and increase the system's stability [40].

3.2. Sluggish diffusion effect

The transformation kinetics of HEAs are lower than those of other alloys because of their less atomic diffusion. Given that HEAs consist of different elements with different melting points, some of these elements are less active due to their low melting point and have a low diffusion coefficient in the lattice. By contrast, the neighboring atoms in one atomic lattice site of these alloys are usually different, thus causing different bonding energies for each atomic site and less diffusion into the lattice [43]. For example, the sluggish diffusion in $Al_{0.1}CoCrFeNi$ HEA locks the dislocation; as a result, the erosion rate of friction stir is increased for this alloy compared with that for stainless steel [44].

3.3. Severe lattice distortion effect

Different from that of pure metals and other alloys, the lattice of HEAs consists of several types of elements, each with a different size. This characteristic leads to severe lattice distortion in HEAs and an increase in their yield strength [45]. For example, a homogenized NbTaTiVZr refractory HEA has a yield strength of (1518 ± 109) MPa [46].

3.4. Cocktail effect

This effect states that the HEAs' properties are strongly dependent on their constituent elements and the interaction between these elements. When several alloying elements are mixed, unexpected properties that cannot be provided by a single element are obtained [47]. For example, replacing Al with transition metals in $Ti_{1.5}ZrNbAl_{0.3}$ HEA lattice provides special features such as good ductility and high strength [48]. In addition, the chromium and niobium elements in $(CoCrFeNi)_{95}Nb_5$ HEA coating structure (fabricated on Q235 steel substrate) form a passive surface layer that is not created by each of these elements alone [4].

4. Electrodeposition

Electrodeposition is a process in which a thin film of metal or alloy is deposited on a conductive substrate. This technique is based on oxidation and reduction (redox) reactions [49–50], and its schematic is shown in Fig. 3.

This method uses an electrolytic cell with four main parts [51]: anode, cathode, electrolyte, and power supply.

Anode and cathode are electrodes where oxidation and reduction reactions take place, respectively. The electrochemical solution of metal salts is an electrolyte that will be coated on the cathode surface. When external current from a power supply is applied to the electrodes, reactions (4) and (5) occur simultaneously, and a thin layer of coating is deposited on the cathode surface [51].

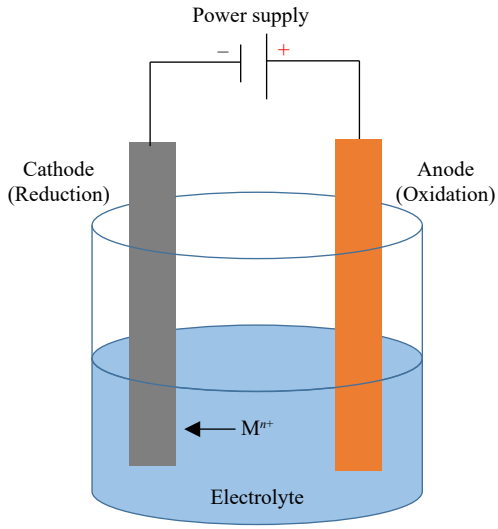

Fig. 3. Schematic of electrodeposition process.

$$M^{n+} + ne^- \rightarrow M(\text{cathodic reaction}) \quad (4)$$

$$M \rightarrow M^{n+} + ne^-(\text{anodic reaction}) \quad (5)$$

The methods for electrodeposition are divided into two types, namely, direct and pulse current [52]. Direct current electrodeposition has been used in various engineering applications. However, pulse electrodeposition has recently attracted more attention than direct current electroplating because of its better current distribution and ion mass transfer and the production of a more suitable microstructure and chemical composition [51].

The use of electrodeposition to generate a HEA coating was first reported by Yao *et al*. [22]. The electrodeposition technique for these alloys is similar to that for traditional alloys; the only difference is that for the former, bath compounds are highly complex and consist of the salts of different metals as the precursor. Table 1 shows the type of electrodeposition process, electrolyte base, bath composition, and crystal structure for HEAs that have been produced by electrodeposition so far.

In this review, the latest studies related to HEA electrodeposition are reported and discussed. The use of direct and pulse electrodeposition methods to produce HEAs is also described. The effect of electrodeposition parameters such as current density, applied potential, and procedure parameters on the film properties are surveyed, and the challenges and future direction of HEA electrodeposition are summarized.

5. Direct and pulse electrodeposition

Direct and pulse current electroplating are the two methods for electrodepositing metals and alloys. Fig. 4 shows a typical direct current plating diagram. In this type of plating, the potential or current is constant over time; that is, the on-time current to total time ratio or duty cycle is 100% [53].

Different from direct current electroplating, pulsed current electrodeposition involves the swift alternating of current or potential between two various values [54]. In addition to current and voltage, three other independent parameters affect the quality of the layer formed with this method: pulse current on-time (t_{on}), peak current density (i_p), and pulse current off-time (t_{off}). The chemical composition and microstructure of these coatings change with these parameters. As shown in Fig. 5, pulse plating can be explained by its variant parameters, namely, peak voltage (V_p), on-time (t_{on}) and off-time (t_{off}), peak-to-peak voltage ($V_{p\text{-}p}$), reference voltage (V_r), duty cycle parameter, and pulse frequency (f). These parameters can specify the changes in the charge and mass transfer processes and affect the coating microstructure by increasing the corrosion resistance, thickness uniformity, and coating surface hardness [54–55].

6. Pulse electrodeposition for HEA production

6.1. Effect of pulse electrodeposition factors on the synthesis of CoCrFeMnNi HEAs

The impact of procedure parameters on the quality of deposition has been delicately investigated. In 2020, Co–Cr–Fe–Mn–Ni HEA coatings were successfully synthesized by pulse electrodeposition [29]. The impact of pulse potential on the coating morphology and composition and the impact of different pulse parameters on the crystallite size, composition, and morphology have also been investigated (Table 2). As indicated by the film properties, the HEA composition and surface morphology are dependent on pulse parameters, such as frequency and duty cycle [29].

The crystal size decreases by increasing the duty cycle at a constant frequency from 50% to 60%. When the frequency is increased from 2500 to 5000 Hz, the crystal size will decrease in the 50% duty cycle but increase in the 60% duty cycle. A previous study first reported the structure and surface morphology of Co–Cr–Fe–Mn–Ni electrodeposited coatings. XRD analysis showed a single solid solution with FCC lattice. Therefore, electrodeposition would be beneficial for creating new metals with remarkable properties [29].

6.2. Effect of pulse electrodeposition parameters on the corrosion properties and wettability of Co–Cr–Fe–Mn–Ni HEA thin films

In 2021, Co–Cr–Fe–Mn–Ni HEA was produced via pulse electrodeposition [30]. The impact of pulse electrodeposition factors on the hydrophobic/hydrophilic behavior and corrosion resistance (corrosion current density (i_{corr}) and oxide coating resistance (R_{coat})) of coatings was studied, and the results are summarized in Table 3. This new alloy system is completely hydrophilic and exhibits good corrosion properties. XRD results showed that the crystal lattice of this layer is completely FCC. As shown in Table 3, the sample coated in 60% duty cycle and 2500 Hz frequency has the highest corrosion resistance [30].

The above studies are the only research conducted in this area. Hence, a huge research gap related to this subject exists.

7. Direct electrodeposition for HEA production

The main research focus in this field is incorporating graphene oxide (GO) into HEAs and investigating the corrosion and magnetic properties of these alloys. In 2008, Yao

Table 1. Successful practices to produce HEAs by electrodeposition: type of electrodeposition and bath composition (DC: Direct current)

Alloy	Type of electrodeposition	Crystal structure	Electrolyte based	Bath composition	Ref.
Bi–Fe–Co–Ni–Mn	DC	Amorphous + FCC (After annealing)	DMF–CH_3CN	$Bi(NO_3)_3$ (0.01 mol·L^{-1}) $FeCl_2$ (0.01 mol·L^{-1}) $CoCl_2$ (0.01 mol·L^{-1}) $NiCl_2$ (0.01 mol·L^{-1}) $MnCl_2$ (0.1 mol·L^{-1})	[22]
Mg–Mn–Fe–Co–Ni–Gd	DC	Amorphous	DMF–CH_3CN	$GdCl_3$ (0.01 mol·L^{-1}) $FeCl_2$ (0.005 mol·L^{-1}) $CoCl_2$ (0.005 mol·L^{-1}) $NiCl_2$ (0.005 mol·L^{-1}) $MnCl_2$ (0.005 mol·L^{-1}) $MgCl_2$ (0.01 mol·L^{-1}) (Solution 1) $GdCl_3$ (0.02 mol·L^{-1}) $FeCl_2$ (0.01 mol·L^{-1}) $CoCl_2$ (0.01 mol·L^{-1}) $NiCl_2$ (0.01 mol·L^{-1}) $MnCl_2$ (0.01 mol·L^{-1}) $MgCl_2$ (0.02 mol·L^{-1}) (Solution 2)	[23]
Al–Cr–Fe–Mn–Ni Al–Cr–Cu–Fe–Mn–Ni	DC	Amorphous + FCC (After annealing)	DMF–CH_3CN	$FeCl_2$ (0.01 mol·L^{-1}) $CrCl_3$ (0.01 mol·L^{-1}) $AlCl_3$ (0.01 mol·L^{-1}) $MnCl_2$ (0.01 mol·L^{-1}) $NiCl_2$ (0.01 mol·L^{-1}) $CuCl_2$ (0.01 mol·L^{-1}) $LiClO_4$ (0.1 mol·L^{-1})	[24]
Al–Fe–Co–Ni–Cu	DC	BCC + FCC	—	$AlCl_3·6H_2O$, $FeCl_2·4H_2O$, $CoCl_2·6H_2O$, $NiCl_2·6H_2O$, $CuCl_2·2H_2O$ By adding graphene oxide (GO)	[25]
Mn–Cr–Fe–Co–Ni	DC	BCC	—	$MnCl_2·4H_2O$ (29.69 g·L^{-1}) $CrCl_3·4H_2O$ (33.30 g·L^{-1}) $FeCl_2·4H_2O$ (7.95 g·L^{-1}) $CoCl_2·6H_2O$ (9.517 g·L^{-1}) $NiCl_2·6H_2O$ (19.02 g·L^{-1}) By adding GO	[26]
Cu–Fe–Ni–Co–Cr	DC	BCC + FCC	—	$FeCl_2·4H_2O$ (7.95 g·L^{-1}) $NiCl_2·6H_2O$ (16.64 g·L^{-1}) $CoCl_2·6H_2O$ (9.52 g·L^{-1}) $CrCl_3·4H_2O$ (37.30 g·L^{-1}) $CuCl_2·2H_2O$ (6.82 g·L^{-1}) By adding GO	[27]
Al–Cr–Fe–Co–Ni–Cu	DC	BCC + FCC	—	$FeCl_2·4H_2O$ (7.95 g·L^{-1}) $NiCl_2·6H_2O$ (16.64 g·L^{-1}) $CoCl_2·6H_2O$ (9.52 g·L^{-1}) $CrCl_3·4H_2O$ (37.30 g·L^{-1}) $CuCl_2·2H_2O$ (6.82 g·L^{-1}) $AlCl_3·6H_2O$ (24.14 g·L^{-1}) By adding GO	[28]
Co–Cr–Fe–Mn–Ni	Pulse current	FCC	DMF–CH_3CN	$CoCl_2$ (0.01 mol·L^{-1}) $CrCl_3$ (0.013 mol·L^{-1}) $FeCl_2$ (0.01 mol·L^{-1}) $MnCl_2$ (0.0103 mol·L^{-1}) $NiCl_2$ (0.001 mol·L^{-1})	[29–30]
Tm–Fe–Co–Ni–Mn	DC	Amorphous	DMSO	$Tm(NO_3)_3$ (0.02 mol·L^{-1}) $FeCl_2$ (0.01 mol·L^{-1}) $CoCl_2$ (0.01 mol·L^{-1}) $NiCl_2$ (0.01 mol·L^{-1}) $MnCl_2$ (0.01 mol·L^{-1}) $LiClO_4$ (0.2 mol·L^{-1})	[31]
Fe–Ni–Co–Bi–Mn	DC	Amorphous	C_3H_7NO and CH_3CN	$Bi(NO_3)_3$ (0.002 mol·L^{-1}) $CoCl_3$ (0.01 mol·L^{-1}) $MnCl_2$ (0.01 mol·L^{-1}) $FeCl_2$ (0.01 mol·L^{-1}) $NiCl_2$ (0.01 mol·L^{-1}) $LiClO_4$ (0.1 mol·L^{-1})	[32]
Fe–Co–Ni–Cr–Mn	DC	FCC	—	—	[33]
Al–Co–Cr–Fe–Ni	DC	—	DMF–CH_3CN	$CrCl_3$ (0.01 mol·L^{-1}) $FeCl_3$ (0.01 mol·L^{-1}) $AlCl_3$ (0.013 mol·L^{-1}) $CoCl_2$ (0.01 mol·L^{-1}) $NiCl_2$ (0.01 mol·L^{-1}) $LiClO_4$ (0.01 mol·L^{-1})	[34]

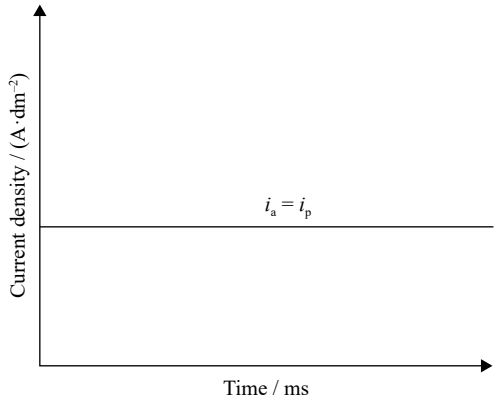

Fig. 4. Direct current electrodeposition waveform (i_a is average current density and i_p is peak current density).

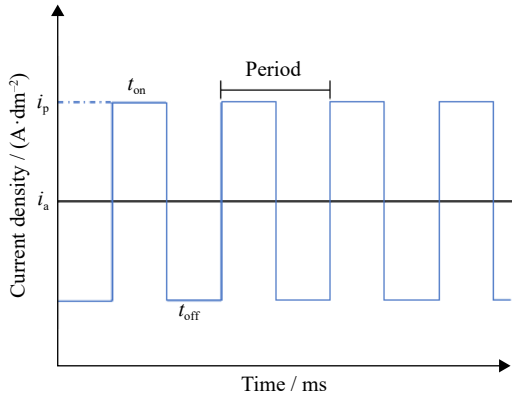

Fig. 5. Example of pulse electrodeposition waveform.

et al. [22] investigated the magnetic properties of Bi–Fe–Co–Ni–Mn HEA film generated using electrochemical methods. SEM examination revealed that the surface was composed of closed grain nanorods with a high aspect ratio are acquired via potentiostatic electrodeposition in the DMF–CH_3CN organic bath [22]. The impact of Bi (III)/TM (II) molar ratios in the organic system and electrodeposition potential on the contents of Bi in the HEA were also studied, and the magnetic and structural studies of this alloy were reported for the first time (Table 4).

$Bi_{19.3}Fe_{20.7}Co_{18.8}Ni_{22.0}Mn_{19.2}$ amorphous layer was obtained via potentiostatic electrodeposition at 2.0 V. After annealing the films under N_2 atmosphere, the XRD and SAED patterns revealed the FCC structure of the solid solution. DTA results confirmed that crystallization was achieved through anneal-

Table 2. Effect of pulse parameters on the morphology and structure of Co–Cr–Fe–Mn–Ni HEA thin films [29]

Coating conditions	Frequency / Hz	Calculated entropy / ($J \cdot K^{-1} \cdot mol^{-1}$)	Cluster size / nm	Morphology	Crystal structure	Crystallite size / nm
Duty cycle: 50% V_{on}: −9 V V_{off}: 1 V	2500	12.04	370–450	Inhomogeneous	FCC	290–370
	5000	11.996		Inhomogeneous	FCC	348–350
Duty cycle: 60% V_{on}: −9 V V_{off}: 1 V	2500	11.86	140–200	Homogeneous	FCC	200–217
	5000	12.46		Homogeneous	FCC	109–140

Note: V_{on} is on-potentials and V_{off} is off-potentials.

Table 3. Effect of pulse parameters on corrosion resistance and wettability of Co–Cr–Fe–Mn–Ni HEA coating [30]

Coating conditions	Frequency / Hz	Calculated entropy / ($J \cdot K^{-1} \cdot mol^{-1}$)	Wettability angle / (°)	i_{corr} / ($\mu A \cdot cm^{-2}$)	Protection efficiency / %	Crystal structure	R_{coat} / ($\Omega \cdot cm^{-2}$)
Duty cycle: 50% V_{on}: −9 V V_{off}: 1 V	2500	12.04	48.16 ± 0.4	0.16	93.00	FCC	79.89
	5000	11.996	44.23 ± 0.2	0.243	89.40	FCC	3609
Duty cycle: 60% V_{on}: −9 V V_{off}: 1 V	2500	11.86	56 ± 0.3	0.067	97.07	FCC	9918
	5000	12.46	41.2 ± 0.2	0.11	95.24	FCC	4899

Table 4. Effect of coating parameters on the magnetic behavior and crystal structure of Bi–Fe–Co–Ni–Mn HEAs [22]

Potential / V	Bi / at%	Bi (II)/TMs (II)	Calculated entropy / ($J \cdot K^{-1} \cdot mol^{-1}$)	Magnetic behavior		Crystal structure	
				Deposited alloy	Annealed alloy	Deposited alloy	Annealed alloy
−1.8	17.1	1:5	13.3	Soft	Hard	Amorphous	FCC
−2.0	19.3	1:5	12.7	Soft	Hard	Amorphous	FCC
−2.2	20.2	1:5	13.0	Soft	Hard	Amorphous	FCC
−2.4	22.7	1:5	12.9	Soft	Hard	Amorphous	FCC
−2.6	16.4	1:5	12.8	Soft	Hard	Amorphous	FCC
−2.0	46.7	2:1	11.8	Soft	Hard	Amorphous	FCC
−2.0	35.5	1:1	12.8	Soft	Hard	Amorphous	FCC
−2.0	21.2	1:2	13.3	Soft	Hard	Amorphous	FCC
−2.0	19.1	1:10	11.9	Soft	Hard	Amorphous	FCC
−2.0	16.3	1:20	12.2	Soft	Hard	Amorphous	FCC

ing at 762 K. Given the soft magnetic properties of the sedimentary layers, the annealed coatings displayed hard magnetic anisotropy. With electrodeposition plating, new materials can be obtained and used in various industries [22].

In 2011, Yao *et al*. [31] presented a facile way to produce the Tm–Fe–Co–Ni–Mn amorphous alloy and then examined its magnetic properties. This study showed that plating is an efficient approach to producing this alloy. The results of this research are shown in Table 5.

All five elements could be deposited simultaneously from the organic system by potentiostatic electrodeposition, and the as-deposited coating was amorphous. This method can be applied to other alloys and oxides. SEM results revealed that closed grains were formed at positive potentials for 10–15 min. Moreover, magnetic studies indicated that the alloys are a type of soft magnetic film, and the magnetic particles were frozen slowly during freezing [31]. In 2014, Li *et al*. [23] produced a Mg–Mn–Fe–Co–Ni–Gd HEA and studied its magnetic properties. A HEA with two hollow and core-shell microstructure was synthesized by electroplating in two different solutions (Table 6).

Two structures, including $Mg_{60.83}Mn_{4.30}Fe_{8.02}Co_{3.51}Ni_{5.52}Gd_{17.82}$ and $Mg_{12.03}Mn_{11.46}Fe_{30.10}Co_{25.17}Ni_{16.15}Gd_{5.09}$, were characterized for this alloy. The surface morphologies can be enhanced by adjusting the metal ion concentration. The results showed that $Mg_{12.03}Mn_{11.46}Fe_{30.10}Co_{25.17}Ni_{16.15}Gd_{5.09}$ alloy was converted from ferromagnetism to diamagnetism at 53 K by applying an external field of 397.89 $kA\cdot m^{-1}$. At 38 K, 795.77 $kA\cdot m^{-1}$ external field is required to achieve this change. Further study on the $Mg_{19.09}Mn_{7.83}Fe_{29.09}Co_{16.93}Ni_{17.91}Gd_{9.15}$ alloy indicated that the critical transition temperature has no linear relationship with the external field. Therefore, the Anderson–Mott transition mechanism was proposed to justify this phenomenon [23]. The results are reported in Table 6.

Table 5. Impact of coating parameters on the properties of Tm–Fe–Co–Ni–Mn alloy [31]

Potential / V	Time / min	Substrate	Surface morphology	Structure	Magnetic properties
−2.1	15	Cu	Nanoflake (50–70 nm)	Amorphous	Soft magnetic and superparamagnetic behavior
−2.5	15	Cu	Nanoflake (50–100 nm)	Amorphous	Soft magnetic and superparamagnetic behavior
−2.1	10	Cu	Compact nanoflake (<100 nm)	Amorphous	Soft magnetic and superparamagnetic behavior
−2.1	30	Cu	Nanoflake (microscale)	Amorphous	Soft magnetic and superparamagnetic behavior
−2.1	15	Ti	Nanoparticle (200–300 nm)	Amorphous	Soft magnetic and superparamagnetic behavior
−2.1	15	Ni	Nanoparticle (100 nm)	Amorphous	Soft magnetic and superparamagnetic behavior

Table 6. Effect of electrodeposition parameters on the structure, surface morphology, and magnetic properties of Mg–Mn–Fe–Co–Ni–Gd HEA [23]

Potential / V	Type of solution	Surface morphology	Structure	Magnetic properties	
				5 K	300 K
−2	1	Hollow hemispheres (diameter: 500–1000 nm; thickness: 10–30 nm)	Amorphous	Hard ferromagnetism	Soft ferromagnetism
−2	2	Core-shell sphere (diameter: 500–1500 nm; thickness: 140–190 nm)	Amorphous	Ferromagnetism	Diamagnetism

In 2014, Zheng *et al*. [32] synthesized Fe–Ni–Co–Bi–Mn HEA coating by electroplating deposition. The authors tried to use the basic electroplating method to prepare Fe–Ni–Co–Bi–Mn HEA thin film. Microscopic analysis of this alloy indicated that the amount of each element in this alloy was more than 5at%, the film has a granular structure, and the crystal grains are approximately 1 mm in size. Therefore, electroplating coating could be an appropriate method to prepare HEA thin films [32].

Aliyu *et al*. [27] produced electroplated, high-entropy Cu–Fe–Ni–Co–Cr coating with graphene oxide (GO) addition and studied its electrochemical, microscopic, and corrosion properties. With GO addition, two different phases were formed: chromium-rich area and chromium-rich and copper-rich area that formed on the coating surface. In the presence of GO, these areas increased the corrosion resistance. Electrochemical studies showed that with the increasing GO addition, the corrosion rate was significantly reduced because the coating structure became uniform [27].

In 2019, Aliyu and Srivastava [26] examined the electrochemical features and microstructure of Mn–Cr–Fe–Co–Ni HEA–GO coatings to determine the impact of GO addition on the microstructure and corrosion behavior of Mn–Cr–Fe–Co–Ni HEA. The amount of GO in the coating structure was controlled by dissolving different GO amounts in the electrolyte bath. The results indicated that the presence of GO increased the corrosion resistance due to the homogenization of the coating microstructure. With GO addition, a Fe–Co–Ni-rich region was created and confined in a Mn–Cr-rich matrix. The presence of a severely oxidizing matrix explains the increase in the corrosion resistance of this coating [26].

The same researchers [25] investigated the corrosion properties and microstructure of Al–Fe–Co–Ni–Cu HEA by adding different GO percentages. The granular morphology in the presence of GO was more compact and finer compared with that in the absence of GO. The coatings consisted of two phases, FCC and BCC, in which the former is rich in Al, and the latter contains Fe, Co, Ni, and Cu. The existence of GO enhanced the amount of FCC phase. Electrochemical

studies in 3.5wt% NaCl solution indicated that this alloy coating generally enhances the corrosion resistance. The highest corrosion protection efficiency was reported for the HEA–GO (31.25 mg/100 mL) coating at 83.41%. With GO addition, the structure became homogeneous with evenly distributed Al, which increased the corrosion resistance. The uniform distribution of Al atoms in the structure prevented galvanic corrosion coupling [25].

In 2019, Aliyu *et al*. [28] investigated the corrosion and microstructural properties of electroplated, high-entropy Al–Cr–Fe–Co–Ni–Cu in the presence of different GO amounts. The electrochemical properties and microstructural changes of this alloy were examined in the presence of different GO amounts in a 3.5wt% NaCl solution. Electrochemical results indicated that the HEA–GO (31.25 mg/100 mL) coating had the highest corrosion resistance and lowest corrosion current density. The corrosion protection efficiency reached 86.92%. Electrochemical impedance spectroscopy (EIS) measurements also confirmed the highest corrosion resistance for the HEA–GO (31.25 mg/100 mL) sample. GO modification on the coating structure has improved the protective efficiency. In the absence of GO, compositional segregation causes the local corrosion of the coating [28]. The results are summarized in Table 7.

Table 7. Summary of the research results by Aliyu and other researchers [25–28]

Type of alloy	Graphene oxide / ($g \cdot L^{-1}$)	C / wt%	Crystal structure	Average crystallite size / nm	i_{corr} / ($\mu A \cdot cm^{-2}$)
CuFeNiCoCr	0	3.89 ± 0.09	BCC + FCC	11.4	101.8 ± 0.032
	0.125	5.93 ± 0.77	BCC + FCC	9.6	27.03 ± 0.033
	0.250	6.24 ± 0.80	BCC + FCC	8.2	22.91 ± 0.074
	0.357	7.63 ± 1.29	BCC + FCC	8.5	13.08 ± 0.042
	0.500	10.06 ± 1.92	BCC + FCC	8.4	6.93 ± 0.089
MnCrFeCoNi	0	4.21 ± 0.35	BCC	47	43.44 ± 0.11
	6.26 mg/100 mL	6.64 ± 0.26	BCC	34	38.94 ± 0.29
	12.5 mg/100 mL	7.39 ± 0.33	BCC	31	32.82 ± 0.28
	18.75 mg/100 mL	8.50 ± 0.34	BCC	30	24.35 ± 0.18
	25 mg/100 mL	9.85 ± 0.46	BCC	25	16.89 ± 0.31
	31.25 mg/100 mL	10.98 ± 0.33	BCC	26	10.89 ± 0.22
AlFeCoNiCu	0	2.02 ± 0.15	BCC + FCC	50.4	123.3 ± 0.14
	6.26 mg/100 mL	2.94 ± 0.07	BCC + FCC	49.1	51.25 ± 0.11
	12.5 mg/100 mL	4.00 ± 0.08	BCC + FCC	45.8	40.29 ± 0.20
	18.75 mg/100 mL	5.73 ± 0.25	BCC + FCC	42.9	33.15 ± 0.21
	25 mg/100 mL	8.30 ± 0.16	BCC + FCC	39.3	29.55 ± 0.16
	31.25 mg/100 mL	9.84 ± 0.12	BCC + FCC	35.8	20.45 ± 0.11
AlCrFeCoNiCu	0	5.51 ± 0.21	BCC + FCC	45.5	93.67 ± 0.13
	6.26 mg/100 mL	8.51 ± 0.28	BCC + FCC	44.7	24.66 ± 0.10
	12.5 mg/100 mL	9.11 ± 0.23	BCC + FCC	39.1	23.52 ± 0.18
	18.75 mg/100 mL	11.21 ± 0.31	BCC + FCC	36.4	15.57 ± 0.12
	25 mg/100 mL	11.98 ± 0.29	BCC + FCC	35.2	13.38 ± 0.11
	31.25 mg/100 mL	12.95 ± 0.30	BCC + FCC	33.9	12.84 ± 0.14

In 2019, Florea and Carcea [33] proposed an electrochemical method for the production of Al–Cu–Fe–Cr–Mn–Ni HEA to create a layer of HEA that could protect the substrate from corrosion, oxidation, and wear in various corrosive environments. Suitable protective properties were obtained by applying this coating [33].

In another study, Cr–Mn–Fe–Co–Ni HEAs were coated on an A36 steel substrate by electrochemical plating. The formed layers are mainly a simple FCC phase with columnar dendrites structure and have an appropriate metallurgical bond with the substrate. The obtained HEA coating has minimal porosity, and the formed phases did not undergo any transformation. Electrochemical studies showed that the alloy coating creates good corrosion resistance for the substrate. In 2020, Kemény *et al*. [34] analyzed the microstructure and corrosion properties of novel Al–Co–Cr–Fe–Ni coating. The coating was first prepared, and its hardness properties and corrosion resistance were examined.

Although the thin layers have different weight ratios of elements, thermodynamic calculations showed that the al-

Table 8. Surface morphology and hardness of Al–Co–Cr–Fe–Ni multicomponent alloy [34]

Sample	Potential / V	Deposition time / min	Stir speed / ($r \cdot min^{-1}$)	Hardness, HV	Structure morphology
A	−2.5	30	50	110	Porous with crack
B	−2.5	60	80	106	Porous with crack
C	−2.5	120	50	86	Coherent and without cracking

loys are of high-entropy type. Further hardness studies (Table 8) revealed that despite its large cracks, the coating is harder than the substrate [34]. Given its homogeneous morphology, only sample C was used to investigate the corrosion properties, as reported in Table 9. The results showed that this alloy coating greatly increased the corrosion resistance of the substrate and is a good protector for the substrate surface [34].

Table 9. Corrosion behavior of substrate and Al–Co–Cr–Fe–Ni multicomponent alloy (sample C) [34]

Immersion time / min	i_{corr} / (μA·cm^{-2})
0	0.211
30	0.126
60	0.927
180	0.0727
300	0.0801

8. Recommendations for future works

In this review, electrodeposition was explored as an efficient method for the production of different types of HEAs with excellent properties due to its cost-effectiveness, availability of its raw materials, less equipment intensiveness, and less complexity than the other approaches. However, the use of this technique is limited by expensive organic baths, the toxicity of some raw materials, and the impossibility of electroplating all metals on special substrates. Table 10 shows some HEAs that have been produced by other meth-

Table 10. HEAs produced by different techniques

Solid-state processing						Liquid state processing					Thin-film deposition process		
Powder atomization	Mechanical alloying	Cold uniaxial pressing	Sintering	Hot pressing	Spark plasma sintering	Arc melting	Induction melting	Directional solidification	Infiltration	Electromagnetic stirring	Magnetron sputtering	Laser deposition	Thermal and plasma spray deposition
$Al_{0.5}$–Co–Cr–Cu–Fe–Ni [56]	$Fe_{0.7}$–$Nb_{0.1}$–$Zr_{0.1}$–$Ti_{0.1}$ [18]	Al–Fe–Ti–Cr–Zn–Cu [57]	Fe–Co–Ni–Cr–Mn [58]	Fe–Co–Cr–Ni–Mn–Al_x [59]	Al–Cu–Ni–Fe–Cr [60]	Hf–Nb–Ti–V–Zr [61]	Hf–Nb–Ta–Ti–Zr [62]	Al–Co–Cr–Cu–Fe–Ni [63]	Co–Cr–Fe–Ni–Ti [64]	$Al_{0.5}$–Co–Cr–Cu–Fe–Ni [65]	Al–Co–Cr–Cu–Fe–Ni [66]	Fe–Ni–Co–Al–Cu [67]	Al–Co–Cr–Fe–Ni [68]
Fe–Co–Cr–Ni [69]	Al–Cu–Ni–Fe–Cr [60]	Hf–Nb–Ta–Ti–Zr [70]	Fe_{20}–Co_{20}–Ni_{20}–Cr_{20}–Mn_{20}–$NaCl_{0.1}$ [58]	Fe–Co–Cr–Ni–Mn–$Ti_{0.1}$–$C_{0.1}$ [71]	Co–Cr–Fe–Ni–$S_{0.5}$ [72]	$Al_{0.1}$–Co–Cr–Fe–Ni [73]	Co–Cr–Fe–Mn–Ni [74]	$Al_{0.7}$–Co–Cr–Fe–Ni [75]	Co–Cr–Fe–Mn–Ni [76]	Al–Cr–Fe–Ni–$Mo_{0.2}$ [77]	Ti–Zr–Hf–Ni–Cu–Co [78]	Al_x–Co–Cr–Fe–Ni [79]	Al–Co–Cr–Cu–Fe–Ni [80]
Cr–Mn–Fe–Co–Ni [81]	Fe_{25}–Co_{25}–Ni_{25}–Al_{10}–Ti_{15} [82]	Co–Cr–Fe–Ni–Mn/WC [83]	$Fe_{18.8}$–$Co_{18.8}$–$Ni_{18.8}$–$Cr_{18.8}$–$Mn_{18.8}$–Al_6 [58]	Ta_{20}–Nb_{20}–Hf_{20}–Zr_{20}–Ti_{20} [84]	(Al–Co–Cr–Fe–Ni)$_{100-x}$$Fe_x$ [85]	Hf–Nb–Ta–Ti–Zr [86]	Al–$Mo_{0.5}$–Nb–$Ta_{0.5}$–Ti–Zr [87]	Co–Cr–Fe–Ni–Cu [88]	Nb–Ta–Ti–V–W [89]	Al–Ti–Cr–Fe–Ni–Cu [90]	Co–Cr–Fe–Ni–$Al_{0.3}$ [91]	$Al_{0.5}$–Co–Cr–Cu–Fe–Ni–$Si_{2.0}$ [92]	Cr–Mn–Fe–Co–Ni [93]
(Cr–Fe–Co–Ni)$_{95}$–Nb_5 [4]	Al–Co–Cr–Fe–Ni–$Ti_{0.5}$ [94]	Co–Cr–Fe–Mn–Ni [58]	Fe_{18}–Co_{18}–Ni_{18}–Cr_{18}–$Mn_{18}Al_{10}$ [58]	Hf–Nb–Ta–Ti–Zr [62]	Co–Cr–Fe–Mn–Ni [95]	Co–Cr–Fe–Ni–Ta_x [96]	$Al_{0.4}$–$Hf_{0.6}$–Nb–Ta–Ti–Zr [97]	Fe–Co–Ni–Al–Si [98]	WC/Co–Cr–Fe–Ni–$Al_{0.2}$ [99]	Hf–Nb–$Si_{0.5}$–Ti–V–Zr [100]	Fe–Co–Ni–Cu–V–Zr–Al [101]	$Al_{0.5}$–Co–Cr–Cu–Fe–Ni–$Si_{1.2}$ [92]	Al_x–Si–Cr–Fe–Co–Ni [102]
Al–Cr–Fe–Co–Ni [103]	Al–Co–Cr–Fe–Ni–Cu [104]	—	Al–Co–Cr–Fe–Ni [105]	Co–Cr–Fe–Mn–Ni/SiC [106]	Al–Fe–Cu–Cr–Mg_x [107]	Fe–Co–Cr–Ni [108]	Al_x–Co–Cr–Fe–Ni [109]	Co–Cr–Fe–Ni–Ti [110]	—	Co–Fe_2–Ni–$Mn_{0.3}$–Al–Cu_x [111]	Cr–Mn–Fe–Co–Ni [112]	Fe–Co–Cr–Ni [113]	$Al_{0.2}$–Ti–Cr–Fe–$Co_{1.5}$–$Ni_{1.5}$–5wt% Ag [114]
Al–Si–$Cr_{1.3}$–$FeO_{0.2}$–$Co_{0.6}$–Ni [115]	$Al_{0.5}$–Fe–$Cu_{0.7}$–Ni–Co–Cr [116]	—	Co–Cr–Fe–Mn–Ni [117]	$Al_{0.1}$–Co–Cr–Fe–Ni [73]	Al–Co–Cr–Fe–Ni [118]	Al–Cr_x–Nb–Ti–V [119]	$Al_{0.3}$–Co–Cr–Fe–Ni [120]	Al–Co–Cr–Fe–$Ni_{2.1}$ [121]	—	$Al_{0.5}$–Cr–Cu–Ni–V [122]	(Al–Cr–Ti–Zr–V) N_x [123]	$Al_{0.5}$–Fe–$Cu_{0.7}$–Ni–Co–Cr [116]	Cr–Mn–Fe–Co–Ni [124]
Al–Si–$Ti_{0.2}$–$Cr_{1.5}$–$Fe_{0.2}$–$Co_{0.6}$–Ni [125]	Al_2–Co–Cr–Cu–Fe–Ni–Ti_x [126]	—	Fe–Co–$Ni_{1.5}$–Cu–$B_{0.5}$–$Y_{0.2}$ [127]	—	$Y_{0.2}$–$Yb_{0.2}$–$Lu_{0.2}$–$Eu_{0.2}$ $Er_{0.2}$ [128]	Al–Nb–Ti–V–Zr_x [129]	Al_2–Co–Cr–Fe–Ni [5]	Fe–Co–Ni–Cr–Al [130]	—	Ti_2–Zr–Hf–$V_{0.5}$–$Mo_{0.2}$ [131]	Cr–Nb–Ti–Mo–Zr [132]	Al_2–Co–Cr–Cu–Fe–Ni–Ti_x [133]	Cr–Fe–Co–Ni–$Mo_{0.2}$ [134]
Al–Ti–Cr–Fe–Co–Ni [7]	Al–Fe–Cu–Cr–Mg_x [107]	—	—	—	—	Co–Cr–Cu–Fe–Ni/TiO [135]	Al_2–Co–Cr–Fe–Ni +3at% Sc [136]	Fe–Co–Ni–Cr–Cu [137]	—	Co–Cr–Fe–Ni–$Nb_{0.25}$ [138]	Cu–Mo–Ta–W–V [139]	6Fe–Ni–Co–Si–Cr–Al–Ti [8]	Al–$Si_{0.2}$–$Ti_{0.2}$–Cr–$Fe_{0.2}$–$Co_{0.6}$–$Ni_{0.2}$ [140]
Cr–Fe–Co–Ni–$Mo_{0.2}$ [134]	Fe–Co–Cr–Ni–Mn–Al_x [59]	—	—	—	—	Ti_x–Zr–V–Nb [141]	$Al_{0.3}$–Co–Cr–Fe–Ni–Mn_x [142]	Fe–Co–Cr–Ni–Cu–$Ti_{0.8}$ [143]	—	Fe–Co–Ni–$Al_{0.2}$–$Si_{0.2}$ [144]	Nb–Mo–Ta–W [145]	Fe–Co–Ni–Cr–Cu [146]	Al–Si–$Ti_{0.2}$–$Cr_{1.5}$–$Fe_{0.2}$–$Co_{0.6}$–Ni [147]

Table 10 (Continued)

Solid-state processing						Liquid state processing				Thin-film deposition process		
—	Fe–Co–Cr–Ni–Mn–Ti_{01}–$C_{0.1}$ [71]	—	—	—	—	—	Al_{25}–Ti_{25}–Ga_{25}–Be_{25} [148]	Co–Cr–Fe–Mn–Ni [149]	—	Co–Cr–Fe–Ni [150]	Al–Mo–Nb–Si–Ta–Ti–V–Zr [151]	Fe–Co–Cr–Ni–$Ti_{0.5}$ [152]	Al–Co–Cr–Fe–Ni–Si [153]
—	Fe_{20}–Co_{20}–Ni_{20}–Cr_{20}–Mn_{20} [58]	—	—	—	—	—	Hf–$Mo_{0.5}$–Nb–Ti–$V_{0.5}$–Si_x [154]	Co–Cr–Fe–Ni–Mn–Pd [155]	—	Al_5–Cr_{12}–Fe_{35}–Mn_{28}–Ni_{20} [156]	Fe–Al–Co–Cu–Ni–V [157]	—	Al–Co–Cr–Fe–Ni–Ti [158]
—	Fe_{20}–Co_{20}–Ni_{20}–Cr_{20}–Mn_{20}–$NaCl_{0.1}$ [58]	—	—	—	—	—	$Al_{0.5}$–Co–Cr–Fe–Ni [159]	Co–Cr–Cu–Ni–$Al_{0.5}$ [160]	—	Al–Cr–Fe–Ni–Mo_x [161]	Al–Cr–Fe–Co–Ni–Cu–V [162]	—	Al–Si–Ti–Cr–Fe–Ni–$Mo_{0.5}$ [163]
—	$Fe_{18.8}$–$Co_{18.8}$–Ni18.8–$Cr_{18.8}$–$Mn_{18.8}$–Al_6 [58]	—	—	—	—	—	—	—	—	Cr–Nb–Ti–Zr–Al_x [164]	Fe–Co–Cr–Ni–$Mo_{0.3}$ [165]	—	Al–Si–Ti–Cr–Fe–Co–Ni–$Mo_{0.5}$ [163]
—	Fe_{18}–Co_{18}–Ni_{18}–Cr_{18}–$Mn_{18}Al_{10}$ [58]	—	—	—	—	—	—	—	—	Al–Co–Cr–Fe–Ni [166]	Cr–Co–Cu–Fe–Ni [167]	—	—
—	Fe–Si–B–Al–Ni–Mo [168]	—	—	—	—	—	—	—	—	Co–Fe–Ni–Ti–V [169]	—	—	—

ods and could be generated by electrodeposition for future works.

9. Conclusion

Electrodeposition is a good technique for fabricating HEAs. In this study, the preparation of HEAs using electrodeposition was surveyed in detail. Various researchers investigated the application of these alloys as a protective layer, either as an alloy or as a composite on different substrates, and the main results were presented in this paper. GO is the only substance that has been used to produce composite layers so far. Other similar materials could be used and investigated in this field.

Conflict of Interest

The authors declare no conflict of interests.

References

[1] J.W. Yeh, S.K. Chen, S.J. Lin, J.Y. Gan, T.S. Chin, T.T. Shun, C.H. Tsau, and S.Y. Chang, Nanostructured high-entropy alloys with multiple principal elements: Novel alloy design concepts and outcomes, *Adv. Eng. Mater.*, 6(2004), No. 5, p. 299.

[2] Z. Cheng, S.Z. Wang, G.L. Wu, J.H. Gao, X.S. Yang, and H.H. Wu, Tribological properties of high-entropy alloys: A review, *Int. J. Miner. Metall. Mater.*, 29(2022), No. 3, p. 389.

[3] W.R. Zhang, P.K. Liaw, and Y. Zhang, Science and technology in high-entropy alloys, *Sci. China Mater.*, 61(2018), No. 1, p. 2.

[4] W.R. Wang, W. Qi, X.L. Zhang, X. Yang, L. Xie, D.Y. Li, and Y.H. Xiang, Superior corrosion resistance-dependent laser energy density in $(CoCrFeNi)_{95}Nb_5$ high entropy alloy coating fabricated by laser cladding, *Int. J. Miner. Metall. Mater.*, 28(2021), No. 5, p. 888.

[5] D. Karlsson, A. Marshal, F. Johansson, M. Schuisky, M. Sahlberg, J.M. Schneider, and U. Jansson, Elemental segregation in an AlCoCrFeNi high-entropy alloy—A comparison between selective laser melting and induction melting, *J. Alloys Compd.*, 784(2019), p. 195.

[6] B.Q. Jin, N.N. Zhang, S. Guan, Y. Zhang, and D.Y. Li, Microstructure and properties of laser re-melting $FeCoCrNiAl_{0.5}Si_x$ high-entropy alloy coatings, *Surf. Coat. Technol.*, 349(2018), p. 867.

[7] A. Meghwal, A. Anupam, B.S. Murty, C.C. Berndt, R.S. Kottada, and A.S.M. Ang, Thermal spray high-entropy alloy coatings: A review, *J. Therm. Spray Technol.*, 29(2020), No. 5, p. 857.

[8] H. Zhang, Y. Pan, Y.Z. He, and H.S. Jiao, Microstructure and properties of 6FeNiCoSiCrAlTi high-entropy alloy coating prepared by laser cladding, *Appl. Surf. Sci.*, 257(2011), No. 6, p. 2259.

[9] C.B. Wei, X.H. Du, Y.P. Lu, H. Jiang, T.J. Li, and T.M. Wang, Novel as-cast $AlCrFe_2Ni_2Ti_{05}$ high-entropy alloy with excellent mechanical properties, *Int. J. Miner. Metall. Mater.*, 27(2020), No. 10, p. 1312.

[10] T.T. Zuo, S.B. Ren, P.K. Liaw, and Y. Zhang, Processing effects on the magnetic and mechanical properties of $FeCoNiAl_{0.2}Si_{0.2}$ high entropy alloy, *Int. J. Miner. Metall. Mater.*, 20(2013), No. 6, p. 549.

[11] B.R. Braeckman, F. Boydens, H. Hidalgo, P. Dutheil, M. Jullien, A.L. Thomann, and D. Depla, High entropy alloy thin films deposited by magnetron sputtering of powder targets, *Thin Solid Films*, 580(2015), p. 71.

[12] M.D. Cropper, Thin films of AlCrFeCoNiCu high-entropy alloy by pulsed laser deposition, *Appl. Surf. Sci.*, 455(2018), p. 153.

[13] X.H. Yan, J.S. Li, W.R. Zhang, and Y. Zhang, A brief review of high-entropy films, *Mater. Chem. Phys.*, 210(2018), p. 12.

[14] N. Malatji, A.P.I. Popoola, T. Lengopeng, and S. Pityana, Effect of Nb addition on the microstructural, mechanical and electrochemical characteristics of AlCrFeNiCu high-entropy alloy, *Int. J. Miner. Metall. Mater.*, 27(2020), No. 10, p. 1332.

[15] M.H.K. Feizabad, E. Sarvestani, and G.R. Khayati, Modeling and optimization of chemical composition of nano/amorphous Fea.Nib.Nbc.Zrd alloy prepared *via* high-energy ball milling with enhanced soft magnetic properties; A mixture design approach, *J. Alloys Compd.*, 841(2020), art. No. 155646.

[16] M.H.K. Feizabad, S. Sharafi, G.R. Khayati, and M. Ranjbar, Modeling of stress relaxation kinetics of amorphous $Fe_{0.7}Nb_{0.1}Zr_{0.1}Ti_{0.1}$ alloy powder: A novel approach based on differential thermal analysis, *Powder Technol.*, 336(2018), p. 441.

[17] M.H.K. Feizabad, G.R. Khayati, S. Sharafi, and M. Ranjbar, Improvement of soft magnetic properties of $Fe_{0.7}Nb_{0.1}Zr_{0.1}Ti_{0.1}$ amorphous alloy: A kinetic study approach, *J. Non-Cryst. Solids*, 493(2018), p. 11.

[18] M.H.K. Feizabad, S. Sharafi, G.R. Khayati, and M. Ranjbar, Effect of process control agent on the structural and magnetic properties of nano/amorphous $Fe_{0.7}Nb_{0.1}Zr_{0.1}Ti_{0.1}$ powders prepared by high energy ball milling, *J. Magn. Magn. Mater.*, 449(2018), p. 297.

[19] C.D. Gómez-Esparza, R. Peréz-Bustamante, J.M. Alvarado-Orozco, J. Muñoz-Saldaña, R. Martínez-Sánchez, J.M. Olivares-Ramírez, and A. Duarte-Moller, Microstructural evaluation and nanohardness of an AlCoCuCrFeNiTi high-entropy alloy, *Int. J. Miner. Metall. Mater.*, 26(2019), No. 5, p. 634.

[20] W.R. Wang, H.F. Xie, L. Xie, H.L. Li, X. Yang, and Y.N. Shen, Anti-penetration performance of high entropy alloy–ceramic gradient composites, *Int. J. Miner. Metall. Mater.*, 25(2018), No. 11, p. 1320.

[21] B. Niu, F. Zhang, H. Ping, N. Li, J.Y. Zhou, L.W. Lei, J.J. Xie, J.Y. Zhang, W.M. Wang, and Z.Y. Fu, Sol-gel autocombustion synthesis of nanocrystalline high-entropy alloys, *Sci. Rep.*, 7(2017), art. No. 3421.

[22] C.Z. Yao, P. Zhang, M. Liu, G.R. Li, J.Q. Ye, P. Liu, and Y.X. Tong, Electrochemical preparation and magnetic study of Bi–Fe–Co–Ni–Mn high entropy alloy, *Electrochimica Acta*, 53(2008), No. 28, p. 8359.

[23] H. Li, H. Sun, C. Wang, B. Wei, C. Yao, Y. Tong, and H. Ma, Controllable electrochemical synthesis and magnetic behaviors of Mg–Mn–Fe–Co–Ni–Gd alloy films, *J. Alloys Compd.*, 598(2014), p. 161.

[24] V. Soare, M. Burada, I. Constantin, D. Mitrică, V. Bădiliță, A. Caragea, and M. Târcolea, Electrochemical deposition and microstructural characterization of AlCrFeMnNi and AlCrCuFeMnNi high entropy alloy thin films, *Appl. Surf. Sci.*, 358(2015), p. 533.

[25] A. Aliyu and C. Srivastava, Microstructure and corrosion performance of AlFeCoNiCu high entropy alloy coatings by addition of graphene oxide, *Materialia*, 8(2019), art. No. 100459.

[26] A. Aliyu and C. Srivastava, Microstructure and corrosion properties of MnCrFeCoNi high entropy alloy-graphene oxide composite coatings, *Materialia*, 5(2019), art. No. 100249.

[27] A. Aliyu, M.Y. Rekha, and C. Srivastava, Microstructure-electrochemical property correlation in electrodeposited CuFeNi-CoCr high-entropy alloy-graphene oxide composite coatings, *Philos. Mag.*, 99(2019), No. 6, p. 718.

[28] A. Aliyu and C. Srivastava, Microstructure-corrosion property correlation in electrodeposited AlCrFeCoNiCu high entropy alloys-graphene oxide composite coatings, *Thin Solid Films*, 686(2019), art. No. 137434.

[29] F. Yoosefan, A. Ashrafi, S.M.M. vaghefi, and I. Constantin, Synthesis of CoCrFeMnNi high entropy alloy thin films by pulse electrodeposition: Part 1: Effect of pulse electrodeposition parameters, *Met. Mater. Int.*, 26(2020), No. 8, p. 1262.

[30] F. Yoosefan, A. Ashrafi, and S.M.M. vaghefi, Characterization of Co–Cr–Fe–Mn–Ni high-entropy alloy thin films synthesized by pulse electrodeposition: Part 2: Effect of pulse electrodeposition parameters on the wettability and corrosion resistance, *Met. Mater. Int.*, 27(2021), No. 1, p. 106.

[31] C.Z. Yao, B.H. Wei, P. Zhang, X.H. Lu, P. Liu, and Y.X. Tong, Facile preparation and magnetic study of amorphous Tm–Fe–Co–Ni–Mn multicomponent alloy nanofilm, *J. Rare Earths*, 29(2011), No. 2, p. 133.

[32] M.S. Zheng, Y. Li, J. Hu, Y. Zhao, and L.J. Yu, Preparation of high entropy alloy thin film fenicobimn by electroplating deposition method, *Mater. Sci. Indian J.*, 11(2014), No. 10, p. 344.

[33] R.M. Florea and I. Carcea, Sustainable anti-corrosive protection technologies for metal products by electrodeposition of HEA layers, *IOP Conf. Ser.: Mater. Sci. Eng.*, 591(2019), No. 1, art. No. 012014.

[34] D.M. Kemény, N.M. Pálfi, and É. Fazakas, Examination of microstructure and corrosion properties of novel AlCoCrFeNi multicomponent alloy, *Mater. Today Proc.*, 45(2021), p. 4250.

[35] J. Mendoza-Canale and J. Marín-Cruz, Corrosion behavior of titanium and nickel-based alloys in HCl and HCl+ H_2S environments, *Int. J. Electrochem. Sci.*, 3(2008), p. 346.

[36] H.B. Muralidhara and Y.A. Naik, Electrochemical deposition of nanocrystalline zinc on steel substrate from acid zincate bath, *Surf. Coat. Technol.*, 202(2008), No. 14, p. 3403.

[37] Y. Zhang, T.T. Zuo, Z. Tang, M.C. Gao, K.A. Dahmen, P.K. Liaw, and Z.P. Lu, Microstructures and properties of high-entropy alloys, *Prog. Mater. Sci.*, 61(2014), p. 1.

[38] M.C. Gao, J.W. Yeh, P.K. Liaw, and Y. Zhang, *High-entropy Alloys: Fundamentals and Applications*, Springer International Publishing Switzerland, 2016.

[39] D.B. Miracle and O.N. Senkov, A critical review of high entropy alloys and related concepts, *Acta Mater.*, 122(2017), p. 448.

[40] J.W. Yeh, Recent progress in high-entropy alloys, *Ann. Chim. Sci. Mat.*, 31(2006), No. 6, p. 633.

[41] A. Takeuchi and A. Inoue, Calculations of mixing enthalpy and mismatch entropy for ternary amorphous alloys, *Mater. Trans., JIM*, 41(2000), No. 11, p. 1372.

[42] Y. Qiu, S. Thomas, D. Fabijanic, A.J. Barlow, H.L. Fraser, and N. Birbilis, Microstructural evolution, electrochemical and corrosion properties of $Al_xCoCrFeNiTi_y$ high entropy alloys, *Mater. Des.*, 170(2019), art. No. 107698.

[43] K.Y. Tsai, M.H. Tsai, and J.W. Yeh, Sluggish diffusion in Co–Cr–Fe–Mn–Ni high-entropy alloys, *Acta Mater.*, 61(2013), No. 13, p. 4887.

[44] R.B. Nair, H.S. Arora, and H.S. Grewal, Enhanced cavitation erosion resistance of a friction stir processed high entropy alloy, *Int. J. Miner. Metall. Mater.*, 27(2020), No. 10, p. 1353.

[45] J.W. Yeh, S.J. Lin, T.S. Chin, J.Y. Gan, S.K. Chen, T.T. Shun, C.H. Tsau, and S.Y. Chou, Formation of simple crystal structures in Cu–Co–Ni–Cr–Al–Fe–Ti–V alloys with multiprincipal metallic elements, *Metall. Mater. Trans. A*, 35(2004), No. 8, p. 2533.

[46] C. Lee, Y. Chou, G. Kim, M.C. Gao, K. An, J. Brechtl, C. Zhang, W. Chen, J.D. Poplawsky, G. Song, Y. Ren, Y.C. Chou, and P.K. Liaw, Lattice-distortion-enhanced yield strength in a refractory high-entropy alloy, *Adv. Mater.*, 32(2020), No. 49, art. No. 2004029.

[47] M.H. Tsai and J.W. Yeh, High-entropy alloys: A critical review, *Mater. Res. Lett.*, 2(2014), No. 3, p. 107.

[48] J.Y. Pang, H.W. Zhang, L. Zhang, Z.W. Zhu, H.M. Fu, H. Li, A.M. Wang, Z.K. Li, and H.F. Zhang, Ductile $Ti_{1.5}ZrNbAl_{0.3}$ refractory high entropy alloy with high specific strength, *Mater. Lett*, 290(2021), art. No. 129428.

[49] B.M. Mundotiya and W. Ullah, Morphology controlled synthesis of the nanostructured gold by electrodeposition techniques. [in] M. Sone and K. Masu, eds., N*ovel Metal Electrodeposition and the Recent Application*, London:

IntechOpen, 2018.
[50] F.W. Bach, A. Laarmann, and T. Wenz, *Modern Surface Technology*, Wiley-VCH Verlag GmbH & Co. KGaA, 2006.
[51] A. Brenner, *Electrodeposition of Alloys—Principles and Practice*, Elsevier Inc., 1963.
[52] N.P. Wasekar, N. Hebalkar, A. Jyothirmayi, B. Lavakumar, M. Ramakrishna, and G. Sundararajan, Influence of pulse parameters on the mechanical properties and electrochemical corrosion behavior of electrodeposited Ni–W alloy coatings with high tungsten content, *Corros. Sci.*, 165(2020), art. No. 108409.
[53] T. Borkar, *Electrodeposition of Nickel Composite Coatings* [Dissertation], Oklahoma State University, 2010.
[54] M.S. Chandrasekar and M. Pushpavanam, Pulse and pulse reverse plating—Conceptual, advantages and applications, *Electrochimica Acta*, 53(2008), No. 8, p. 3313.
[55] Endres, Frank, Andrew Abbott, and Douglas R. MacFarlane, eds. *Electrodeposition from ionic liquids*. John Wiley & Sons, (2017).
[56] Y. Brif, M. Thomas, and I. Todd, The use of high-entropy alloys in additive manufacturing, *Scr. Mater.*, 99(2015), p. 93.
[57] S. Varalakshmi, G.A. Rao, M. Kamaraj, and B.S. Murty, Hot consolidation and mechanical properties of nanocrystalline equiatomic AlFeTiCrZnCu high entropy alloy after mechanical alloying, *J. Mater. Sci.*, 45(2010), No. 19, p. 5158.
[58] M.D. Alcalá, C. Real, I. Fombella, I. Trigo, and J.M. Córdoba, Effects of milling time, sintering temperature, Al content on the chemical nature, microhardness and microstructure of mechanochemically synthesized FeCoNiCrMn high entropy alloy, *J. Alloys Compd.*, 749(2018), p. 834.
[59] H. Cheng, X.Q. Liu, Q.H. Tang, W.G. Wang, X.H. Yan, and P.Q. Dai, Microstructure and mechanical properties of FeCoCrNiMnAl$_x$ high-entropy alloys prepared by mechanical alloying and hot-pressed sintering, *J. Alloys Compd.*, 775(2019), p. 742.
[60] A.I. Yurkova, V.V. Cherniavsky, V. Bolbut, M. Krüger, and I. Bogomol, Structure formation and mechanical properties of the high-entropy AlCuNiFeCr alloy prepared by mechanical alloying and spark plasma sintering, *J. Alloys Compd.*, 786(2019), p. 139.
[61] A. Poulia, E. Georgatis, C. Mathiou, and A.E. Karantzalis, Phase segregation discussion in a $Hf_{25}Zr_{30}Ti_{20}Nb_{15}V_{10}$ high entropy alloy: The effect of the high melting point element, *Mater. Chem. Phys.*, 210(2018), p. 251.
[62] J. Málek, J. Zýka, F. Lukáč, M. Vilémová, T. Vlasák, J. Čížek, O. Melikhova, A. Macháčková, and H.S. Kim, The effect of processing route on properties of HfNbTaTiZr high entropy alloy, *Materials* (*Basel*), 12(2019), No. 23, art. No. 4022.
[63] G.H. Meng, N.A. Protasova, E.P. Kruglov, X. Lin, H. Xie, and X. Ding, Solidification behavior and morphological evolution in laser surface forming of AlCoCrCuFeNi multi-layer high-entropy alloy coatings on AZ91D, *J. Alloys Compd.*, 772(2019), p. 994.
[64] M.A. Haq, N.S.A. Eom, N. Su, H. Lee, T.S. Kim, and B.S. Kim, Powder interface modification for synthesis of core-shell structured CoCrFeNiTi high entropy alloy composite, *Appl. Surf. Sci.*, 506(2020), art. No. 144925.
[65] Y.Y. Du, Y.P. Lu, T.M. Wang, T.J. Li, and G.L. Zhang, Effect of electromagnetic stirring on microstructure and properties of Al0.5CoCrCuFeNi alloy, *Procedia Eng.*, 27(2012), p. 1129.
[66] L. Xie, P. Brault, A.L. Thomann, X. Yang, Y. Zhang, and G.Y. Shang, Molecular dynamics simulation of Al–Co–Cr–Cu–Fe–Ni high entropy alloy thin film growth, *Intermetallics*, 68(2016), p. 78.
[67] G. Jin, Z.B. Cai, Y.J. Guan, X.F. Cui, Z. Liu, Y. Li, M.L. Dong, and D. zhang, High temperature wear performance of laser-cladded FeNiCoAlCu high-entropy alloy coating, *Appl. Surf. Sci.*, 445(2018), p. 113.
[68] A. Meghwal, A. Anupam, V. Luzin, C. Schulz, C. Hall, B.S. Murty, R.S. Kottada, C.C. Berndt, and A.S.M. Ang, Multiscale mechanical performance and corrosion behaviour of plasma sprayed AlCoCrFeNi high-entropy alloy coatings, *J. Alloys Compd.*, 854(2021), art. No. 157140.
[69] P. Cui, Y.M. Ma, L.J. Zhang, M.D. Zhang, J.T. Fan, W.Q. Dong, P.F. Yu, and G. Li, Microstructure and mechanical behaviors of CoFeNiMnTi$_x$Al$_{1-x}$ high entropy alloys, *Mater. Sci. Eng. A*, 731(2018), p. 124.
[70] J. Málek, J. Zýka, F. Lukáč, J. Čížek, L. Kunčická, and R. Kocich, Microstructure and mechanical properties of sintered and heat-treated HfNbTaTiZr high entropy alloy, *Metals*, 9(2019), No. 12, art. No. 1324.
[71] X.Q. Liu, H. Cheng, Z.J. Li, H. Wang, F. Chang, W.G. Wang, Q.H. Tang, and P.Q. Dai, Microstructure and mechanical properties of FeCoCrNiMnTi$_{0.1}$C$_{0.1}$ high-entropy alloy produced by mechanical alloying and vacuum hot pressing sintering, *Vacuum*, 165(2019), p. 297.
[72] A.J. Zhang, J.S. Han, B. Su, and J.H. Meng, A promising new high temperature self-lubricating material: CoCrFeNiS$_{0.5}$ high entropy alloy, *Mater. Sci. Eng. A*, 731(2018), p. 36.
[73] P.F. Yu, H. Cheng, L.J. Zhang, H. Zhang, Q. Jing, M.Z. Ma, P.K. Liaw, G. Li, and R.P. Liu, Effects of high pressure torsion on microstructures and properties of an Al$_{0.1}$CoCrFeNi high-entropy alloy, *Mater. Sci. Eng. A*, 655(2016), p. 283.
[74] F. Xiong, R.D. Fu, Y.J. Li, and D.L. Sang, Effects of nitrogen alloying and friction stir processing on the microstructures and mechanical properties of CoCrFeMnNi high-entropy alloys, *J. Alloys Compd.*, 822(2020), art. No. 153512.
[75] G. Liu, L. Liu, X.W. Liu, Z.J. Wang, Z.H. Han, G.J. Zhang, and A. Kostka, Microstructure and mechanical properties of Al$_{0.7}$CoCrFeNi high-entropy-alloy prepared by directional solidification, *Intermetallics*, 93(2018), p. 93.
[76] J.G. Kim, J.M. Park, J.B. Seol, J. Choe, J.H. Yu, S.S. Yang, and H.S. Kim, Nano-scale solute heterogeneities in the ultrastrong selectively laser melted carbon-doped CoCrFeMnNi alloy, *Mater. Sci. Eng. A*, 773(2020), art. No. 138726.
[77] Y. Dong, D.X. Qiao, H.Z. Zhang, Y.P. Lu, T.M. Wang, and T.J. Li, Microstructure evolution and hardness of AlCrFeNi$_x$Mo$_{0.2}$ high entropy alloy, *Mater. Sci. Forum*, 849(2016), p. 40.
[78] Y.S. Kim, H.J. Park, S.C. Mun, E. Jumaev, S.H. Hong, G. Song, J.T. Kim, Y.K. Park, K.S. Kim, S.I. Jeong, Y.H. Kwon, and K.B. Kim, Investigation of structure and mechanical properties of TiZrHfNiCuCo high entropy alloy thin films synthesized by magnetron sputtering, *J. Alloys Compd.*, 797(2019), p. 834.
[79] Q. Chao, T.T. Guo, T. Jarvis, X.H. Wu, P. Hodgson, and D. Fabijanic, Direct laser deposition cladding of Al$_x$CoCrFeNi high entropy alloys on a high-temperature stainless steel, *Surf. Coat. Technol.*, 332(2017), p. 440.
[80] T.M. Yue, H. Xie, X. Lin, H.O. Yang, and G.H. Meng, Microstructure of laser re-melted AlCoCrCuFeNi high entropy alloy coatings produced by plasma spraying, *Entropy*, 15(2013), No. 12, p. 2833.
[81] Y. Tian, C.Y. Lu, Y.F. Shen, and X.M. Feng, Microstructure and corrosion property of CrMnFeCoNi high entropy alloy coating on Q235 substrate *via* mechanical alloying method, *Surf. Interfaces*, 15(2019), p. 135.
[82] Z.Q. Fu, L. Jiang, J.L. Wardini, B.E. MacDonald, H.M. Wen, W. Xiong, *et al.*, A high-entropy alloy with hierarchical nanoprecipitates and ultrahigh strength, *Sci. Adv.*, 4(2018), art. No. eaat8712.
[83] I.L. Velo, F.J. Gotor, M.D. Alcalá, C. Real, and J.M. Córdoba, Fabrication and characterization of WC–HEA cemented

carbide based on the CoCrFeNiMn high entropy alloy, *J. Alloys Compd.*, 746(2018), p. 1.

[84] N. Larianovsky, A. Katz-Demyanetz, E. Eshed, and M. Regev, Microstructure, tensile and creep properties of $Ta_{20}Nb_{20}Hf_{20}Zr_{20}Ti_{20}$ high entropy alloy, *Materials* (*Basel*), 10(2017), No. 8, art. No. 883.

[85] L. Guo, D.H. Xiao, W.Q. Wu, S. Ni, and M. Song, Effect of Fe on microstructure, phase evolution and mechanical properties of $(AlCoCrFeNi)_{100-x}Fe_x$ high entropy alloys processed by spark plasma sintering, *Intermetallics*, 103(2018), p. 1.

[86] C. Yang, K. Aoyagi, H.K. Bian, and A. Chiba, Microstructure evolution and mechanical property of a precipitation-strengthened refractory high-entropy alloy HfNbTaTiZr, *Mater. Lett.*, 254(2019), p. 46.

[87] T.E. Whitfield, H.J. Stone, C.N. Jones, and N.G. Jones, Microstructural degradation of the $AlMo_{0.5}NbTa_{0.5}TiZr$ refractory metal high-entropy superalloy at elevated temperatures, *Entropy* (*Basel*), 23(2021), No. 1, art. No. 80.

[88] H.T. Zheng, R.R. Chen, G. Qin, X.Z. Li, Y.Q. Su, H.S. Ding, J.J. Guo, and H.Z. Fu, Microstructure evolution, Cu segregation and tensile properties of CoCrFeNiCu high entropy alloy during directional solidification, *J. Mater. Sci. Technol.*, 38(2020), p. 19.

[89] A.O. Moghaddam, J. Pasandideh, A. Abdollahzadeh, N.A. Shaburova, and E. Trofimov, On the application of NbTaTiVW refractory high entropy alloy particles in the manufacturing process of WC based matrix body drill bits, *Int. J. Refract. Met. Hard Mater.*, 99(2021), art. No. 105608.

[90] J.H. Pi, Y. Pan, L. Zhang, and H. Zhang, Microstructure and property of AlTiCrFeNiCu high-entropy alloy, *J. Alloys Compd.*, 509(2011), No. 18, p. 5641.

[91] W.B. Liao, S. Lan, L.B. Gao, H.T. Zhang, S. Xu, J. Song, X.L. Wang, and Y. Lu, Nanocrystalline high-entropy alloy (CoCrFeNiAl$_{0.3}$) thin-film coating by magnetron sputtering, *Thin Solid Films*, 638(2017), p. 383.

[92] M. Dada, P. Popoola, and N. Mathe, Recent advances of high entropy alloys for aerospace applications: A review, *World J. Eng.*, 2021, https://doi.org/10.1108/WJE-01-2021-00400

[93] J.K. Xiao, H. Tan, Y.Q. Wu, J. Chen, and C. Zhang, Microstructure and wear behavior of FeCoNiCrMn high entropy alloy coating deposited by plasma spraying, *Surf. Coat. Technol.*, 385(2020), art. No. 125430.

[94] I. Moravcik, J. Cizek, P. Gavendova, S. Sheikh, S. Guo, and I. Dlouhy, Effect of heat treatment on microstructure and mechanical properties of spark plasma sintered $AlCoCrFeNiTi_{0.5}$ high entropy alloy, *Mater. Lett.*, 174(2016), p. 53.

[95] L. Yang, C.C. Zhao, W.W. Zhu, Z. Cheng, P.B. Wei, and F.Z. Ren, Microstructure, mechanical properties, and sliding wear behavior of oxide-dispersion-strengthened FeMnNi alloy fabricated by spark plasma sintering, *Metall. Mater. Trans. A*, 51(2020), No. 6, p. 2796.

[96] W.Y. Huo, H. Zhou, F. Fang, X.F. Zhou, Z.H. Xie, and J.Q. Jiang, Microstructure and properties of novel $CoCrFeNiTa_x$ eutectic high-entropy alloys, *J. Alloys Compd.*, 735(2018), p. 897.

[97] O.N. Senkov, S.V. Senkova, and C. Woodward, Effect of aluminum on the microstructure and properties of two refractory high-entropy alloys, *Acta Mater.*, 68(2014), p. 214.

[98] T.T. Zuo, X. Yang, P.K. Liaw, and Y. Zhang, Influence of Bridgman solidification on microstructures and magnetic behaviors of a non-equiatomic FeCoNiAlSi high-entropy alloy, *Intermetallics*, 67(2015), p. 171.

[99] G.N. Zhang, X. Yang, Z.C. Yang, Y. Li, G. He, and J.T. Li, Preparation of $WC/CoCrFeNiAl_{0.2}$ high-entropy-alloy composites by high-gravity combustion synthesis, *Int. J. Miner. Metall. Mater.*, 27(2020), No. 2, p. 244.

[100] Y. Zhang, Y. Liu, Y.X. Li, X. Chen, and H.W. Zhang, Microstructure and mechanical properties of a new refractory HfNb$Si_{0.5}$TiVZr high entropy alloy, *Mater. Sci. Forum*, 849(2016), p. 76.

[101] L. Liu, J.B. Zhu, C. Hou, J.C. Li, and Q. Jiang, Dense and smooth amorphous films of multicomponent FeCoNiCuVZrAl high-entropy alloy deposited by direct current magnetron sputtering, *Mater. Des.*, 46(2013), p. 675.

[102] J.K. Xiao, Y.Q. Wu, J. Chen, and C. Zhang, Microstructure and tribological properties of plasma sprayed $FeCoNiCrSiAl_x$ high entropy alloy coatings, *Wear*, 448-449(2020), art. No. 203209.

[103] K.C. Cheng, J.H. Chen, S. Stadler, and S.H. Chen, Properties of atomized AlCoCrFeNi high-entropy alloy powders and their phase-adjustable coatings prepared *via* plasma spray process, *Appl. Surf. Sci.*, 478(2019), p. 478.

[104] S. Thangaraju, E. Bouzy, and A. Hazotte, Phase stability of a mechanically alloyed CoCrCuFeNi high entropy alloy , *Adv. Eng. Mater.*, 19(2017), No. 8, art. No. 1700095.

[105] V. Shivam, J. Basu, V.K. Pandey, Y. Shadangi, and N.K. Mukhopadhyay, Alloying behaviour, thermal stability and phase evolution in quinary AlCoCrFeNi high entropy alloy, *Adv. Powder Technol.*, 29(2018), No. 9, p. 2221.

[106] Ł. Rogal, D. Kalita, A. Tarasek, P. Bobrowski, and F. Czerwinski, Effect of SiC nano-particles on microstructure and mechanical properties of the CoCrFeMnNi high entropy alloy, *J. Alloys Compd.*, 708(2017), p. 344.

[107] O. Maulik, D. Kumar, S. Kumar, D.M. Fabijanic, and V. Kumar, Structural evolution of spark plasma sintered AlFeCuCrMg_x (x = 0, 0.5, 1, 1.7) high entropy alloys, *Intermetallics*, 77(2016), p. 46.

[108] S. Li, S. Lei, Y.B. Wu, S.S. Hu, Y.F. Liu, and H.L. Xu, Effect of Ti content on magnetic and electrochemical corrosion properties of FeCoCrNi high entropy alloys, *ECS J. Solid State Sci. Technol.*, 10(2021), No. 3, art. No. 033003.

[109] M. Izadi, M. Soltanieh, S. Alamolhoda, S.M.S. Aghamiri, and M. Mehdizade, Microstructural characterization and corrosion behavior of Al_xCoCrFeNi high entropy alloys, *Mater. Chem. Phys.*, 273(2021), art. No. 124937.

[110] A.C. Yeh, Y.J. Chang, C.W. Tsai, Y.C. Wang, J.W. Yeh, and C.M. Kuo, On the solidification and phase stability of a Co–Cr–Fe–Ni–Ti high-entropy alloy, *Metall. Mater. Trans. A*, 45(2014), No. 1, p. 184.

[111] M. Zhu, C. Zhang, K. Li, Y.Q. Liu, M. Zhang, L.J. Yao, and Z.Y. Jian, A novel $CoFe_2NiMn_{0.3}AlCu_x$ high-entropy alloy with excellent magnetic properties and good mechanical properties, *Acta Metall. Sinica Engl. Lett.*, 34(2021), No. 11, p. 1557.

[112] L.Z. Medina, L. Riekehr, and U. Jansson, Phase formation in magnetron sputtered CrMnFeCoNi high entropy alloy, *Surf. Coat. Technol.*, 403(2020), art. No. 126323.

[113] S.Y. Duan, X.H. Zhan, M.Y. Wu, H.C. Bu, and Q.Y. Gao, Analysis of elements non-uniform distribution of FeCoCrNi high-entropy alloy coatings on Ti–6Al–4V surface by laser cladding, *Met. Mater. Int.*, 27(2021), No. 3, p. 467.

[114] H. Li, J.L. Li, C.Q. Yan, X.F. Zhang, and D.S. Xiong, Microstructure and tribological properties of plasma-sprayed $Al_{0.2}Co_{1.5}CrFeNi_{1.5}$.Ti–Ag composite coating from 25 to 750°C, *J. Mater. Eng. Perform.*, 29(2020), No. 3, p. 1640.

[115] W.L. Hsu, H. Murakami, H. Araki, M. Watanabe, S. Kuroda, A.C. Yeh, and J.W. Yeh, A study of $NiCo_{0.6}Fe_{0.2}Cr_xSiAlTi_y$ High-entropy alloys for applications as a high-temperature protective coating and a bond coat in thermal barrier coating systems, *J. Electrochem. Soc.*, 165(2018), No. 9, p. C524.

[116] C. Ni, Y. Shi, J. Liu, and G.Z. Huang, Characterization of Al0.5FeCu0.7NiCoCr high-entropy alloy coating on aluminum alloy by laser cladding, *Opt. Laser Technol.*, 105(2018), p. 257.

[117] R.B. Mane, R. Y, and B.B. Panigrahi, Sintering mechanism of CoCrFeMnNi high-entropy alloy powders, *Powder Metall.*, 61(2018), No. 2, p. 131.
[118] Y.S. Geng, H. Tan, L. Wang, A.K. Tieu, J. Chen, J. Cheng, and J. Yang, Nano-coupled heterostructure induced excellent mechanical and tribological properties in AlCoCrFeNi high entropy alloy, *Tribol. Int.*, 154(2021), art. No. 106662.
[119] N.D. Stepanov, N.Y. Yurchenko, D.V. Skibin, M.A. Tikhonovsky, and G.A. Salishchev, Structure and mechanical properties of the $AlCr_xNbTiV$ (x = 0, 0.5, 1, 1.5) high entropy alloys, *J. Alloys Compd.*, 652(2015), p. 266.
[120] T.T. Shun and Y.C. Du, Microstructure and tensile behaviors of FCC $Al_{0.3}CoCrFeNi$ high entropy alloy, *J. Alloys Compd.*, 479(2009), No. 1-2, p. 157.
[121] H.T. Zheng, R.R. Chen, G. Qin, X.Z. Li, Y.Q. Su, H.S. Ding, J.J. Guo, and H.Z. Fu, Phase separation of $AlCoCrFeNi_{2.1}$ eutectic high-entropy alloy during directional solidification and their effect on tensile properties, *Intermetallics*, 113(2019), art. No. 106569.
[122] J.J. Yi, S. Tang, M.Q. Xu, L. Yang, L. Wang, and L. Zeng, A novel $Al_{0.5}CrCuNiV$ 3d transition metal high-entropy alloy: Phase analysis, microstructure and compressive properties, *J. Alloys Compd.*, 846(2020), art. No. 156466.
[123] L.Q. Chen, W. Li, P. Liu, K. Zhang, F.C. Ma, X.H. Chen, H.L. Zhou, and X.K. Liu, Microstructure and mechanical properties of $(AlCrTiZrV)N_x$ high-entropy alloy nitride films by reactive magnetron sputtering, *Vacuum*, 181(2020), art. No. 109706.
[124] S. Yin, W.Y. Li, B. Song, X.C. Yan, M. Kuang, Y.X. Xu, K. Wen, and R. Lupoi, Deposition of FeCoNiCrMn high entropy alloy (HEA) coating *via* cold spraying, *J. Mater. Sci. Technol.*, 35(2019), No. 6, p. 1003.
[125] L.M. Wang, C.C. Chen, J.W. Yeh, and S.T. Ke, The microstructure and strengthening mechanism of thermal spray coating $Ni_xCo_{0.6}Fe_{0.2}Cr_ySi_zAlTi_{0.2}$ high-entropy alloys, *Mater. Chem. Phys.*, 126(2011), No. 3, p. 880.
[126] X.W. Qiu, Microstructure, hardness and corrosion resistance of $Al_2CoCrCuFeNiTi_x$ high-entropy alloy coatings prepared by rapid solidification, *J. Alloys Compd.*, 735(2018), p. 359.
[127] C.W. Wang, H.M. Wang, G.R. Li, M. Liu, D. Zhang, H.R. Wen, W.X. Ren, L.P. Gao, and J.J. Chen, Microwave vacuum sintering of $FeCoNi_{1.5}CuB_{0.5}Y_{0.2}$ high-entropy alloy: Effect of heat treatment on microstructure and mechanical property, *Vacuum*, 181(2020), art. No. 109738.
[128] G.R. Zhang and Y.Q. Wu, High-entropy transparent ceramics: Review of potential candidates and recently studied cases, *Int. J. Appl. Ceram. Technol.*, 19(2022), No. 2, p. 644.
[129] N.Y. Yurchenko, N.D. Stepanov, S.V. Zherebtsov, M.A. Tikhonovsky, and G.A. Salishchev, Structure and mechanical properties of B2 ordered refractory $AlNbTiVZr_x$ (x = 0–1.5) high-entropy alloys, *Mater. Sci. Eng. A*, 704(2017), p. 82.
[130] H.B. Cui, H.Y. Wang, J.Y. Wang, and H.Z. Fu, Microstructure and microsegregation in directionally solidified FeCoNiCrAl high entropy alloy, *Adv. Mater. Res.*, 189-193(2011), p. 3840.
[131] Y.P. Lu, H.F. Huang, X.Z. Gao, C.L. Ren, J. Gao, H.Z. Zhang, S.J. Zheng, Q.Q. Jin, Y.H. Zhao, C.Y. Lu, T.M. Wang, and T.J. Li, A promising new class of irradiation tolerant materials: $Ti_2ZrHfV_{0.5}Mo_{0.2}$ high-entropy alloy, *J. Mater. Sci. Technol.*, 35(2019), No. 3, p. 369.
[132] J.J. Wang, S.F. Kuang, X. Yu, L.Q. Wang, and W.J. Huang, Tribo-mechanical properties of CrNbTiMoZr high-entropy alloy film synthesized by direct current magnetron sputtering, *Surf. Coat. Technol.*, 403(2020), art. No. 126374.
[133] X.W. Qiu, Structure and electrochemical properties of laser cladding $Al_2CoCrCuFeNiTi_x$ high-entropy alloy coatings, *Met. Mater. Int.*, 26(2020), No. 7, p. 998.
[134] T.C. Li, Y. Liu, B. Liu, W.M. Guo, and L.Y. Xu, Microstructure and wear behavior of $FeCoCrNiMo_{0.2}$ high entropy coatings prepared by air plasma spray and the high velocity oxy-fuel spray processes, *Coatings*, 7(2017), No. 9, art. No. 151.
[135] Q.D. Qin, J.B. Qu, Y.E. Hu, Y.J. Wu, and X.D. Su, Microstructural characterization and oxidation resistance of multicomponent equiatomic CoCrCuFeNi–TiO high-entropy alloy, *Int. J. Miner. Metall. Mater.*, 25(2018), No. 11, p. 1286.
[136] K.V. Yusenko, S. Riva, W.A. Crichton, K. Spektor, E. Bykova, A. Pakhomova, A. Tudball, I. Kupenko, A. Rohrbach, S. Klemme, F. Mazzali, S. Margadonna, N.P. Lavery, and S.G.R. Brown, High-pressure high-temperature tailoring of High Entropy Alloys for extreme environments, *J. Alloys Compd.*, 738(2018), p. 491.
[137] J.B. Cheng, X.B. Liang, and B.S. Xu, Effect of Nb addition on the structure and mechanical behaviors of CoCrCuFeNi high-entropy alloy coatings, *Surf. Coat. Technol.*, 240(2014), p. 184.
[138] F. He, Z.J. Wang, S.Z. Niu, Q.F. Wu, J.J. Li, J.C. Wang, C.T. Liu, and Y.Y. Dang, Strengthening the $CoCrFeNiNb_{0.25}$ high entropy alloy by FCC precipitate, *J. Alloys Compd.*, 667(2016), p. 53.
[139] S. Alvi, D.M. Jarzabek, M.G. Kohan, D. Hedman, P. Jenczyk, M.M. Natile, A. Vomiero, and F. Akhtar, Synthesis and mechanical characterization of a CuMoTaWV high-entropy film by magnetron sputtering, *ACS Appl. Mater. Interfaces*, 12(2020), No. 18, p. 21070.
[140] W.L. Hsu, H. Murakami, J.W. Yeh, A.C. Yeh, and K. Shimoda, On the study of thermal-sprayed $Ni_{0.2}Co_{0.6}Fe_{0.2}CrSi_{0.2}AlTi_{0.2}$ HEA overlay coating, *Surf. Coat. Technol.*, 316(2017), p. 71.
[141] T.D. Huang, S.Y. Wu, H. Jiang, Y.P. Lu, T.M. Wang, and T.J. Li, Effect of Ti content on microstructure and properties of Ti_xZrVNb refractory high-entropy alloys, *Int. J. Miner. Metall. Mater.*, 27(2020), No. 10, p. 1318.
[142] S.K. Wong, T.T. Shun, C.H. Chang, and C.F. Lee, Microstructures and properties of $Al_{0.3}CoCrFeNiMn_x$ high-entropy alloys, *Mater. Chem. Phys.*, 210(2018), p. 146.
[143] Y.K. Xu, C.L. Li, Z.H. Huang, Y.N. Chen, and L.X. Zhu, Microstructure evolution and mechanical properties of $FeCoCrNiCuTi_{0.8}$ high-entropy alloy prepared by directional solidification, *Entropy* (*Basel*), 22(2020), No. 7, art. No. 786.
[144] Y. Zhang, *High-Entropy Materials*, Springer Nature Singapore, 2(2019), p. 65.
[145] H. Kim, S. Nam, A. Roh, M. Son, M.H. Ham, J.H. Kim, and H. Choi, Mechanical and electrical properties of NbMoTaW refractory high-entropy alloy thin films, *Int. J. Refract. Met. Hard Mater.*, 80(2019), p. 286.
[146] H. Zhang, Y. Pan, and Y.Z. He, Synthesis and characterization of FeCoNiCrCu high-entropy alloy coating by laser cladding, *Mater. Des.*, 32(2011), No. 4, p. 1910.
[147] W.L. Hsu, Y.C. Yang, C.Y. Chen, and J.W. Yeh, Thermal sprayed high-entropy $NiCo_{0.6}Fe_{0.2}Cr_{1.5}SiAlTi_{0.2}$ coating with improved mechanical properties and oxidation resistance, *Intermetallics*, 89(2017), p. 105.
[148] É. Fazakas, J.Q. Wang, V. Zadorozhnyy, D.V. Louzguine-Luzgin, and L.K. Varga, Microstructural evolution and corrosion behavior of $Al_{25}Ti_{25}Ga_{25}Be_{25}$ equi-molar composition alloy, *Mater. Corros.*, 65(2014), No. 7, p. 691.
[149] H.T. Zheng, Q. Xu, R.R. Chen, G. Qin, X.Z. Li, Y.Q. Su, J.J. Guo, and H.Z. Fu, Microstructure evolution and mechanical property of directionally solidified CoCrFeMnNi high entropy alloy, *Intermetallics*, 119(2020), art. No. 106723.
[150] J. Wang, T. Guo, J.S. Li, W.J. Jia, and H.C. Kou, Microstructure and mechanical properties of non-equilibrium solidified CoCrFeNi high entropy alloy, *Mater. Chem. Phys.*, 210(2018), p. 192.

[151] M.H. Tsai, J.W. Yeh, and J.Y. Gan, Diffusion barrier properties of AlMoNbSiTaTiVZr high-entropy alloy layer between copper and silicon, *Thin Solid Films*, 516(2008), No. 16, p. 5527.

[152] Y. Zhang, T.F. Han, M. Xiao, and Y.F. Shen, Effect of process parameters on the microstructure and properties of laser-clad $FeNiCoCrTi_{0.5}$ high-entropy alloy coating, *Int. J. Miner. Metall. Mater.*, 27(2020), No. 5, p. 630.

[153] L.H. Tian, M. Fu, and W. Xiong, Microstructural evolution of AlCoCrFeNiSi high-entropy alloy powder during mechanical alloying and its coating performance, *Materials* (*Basel*), 11(2018), No. 2, art. No. 320.

[154] Y. Liu, Y. Zhang, H. Zhang, N.J. Wang, X. Chen, H.W. Zhang, and Y.X. Li, Microstructure and mechanical properties of refractory $HfMo_{0.5}NbTiV_{0.5}Si_x$ high-entropy composites, *J. Alloys Compd.*, 694(2017), p. 869.

[155] Y.M. Tan, J.S. Li, J. Wang, and H.C. Kou, Seaweed eutectic-dendritic solidification pattern in a CoCrFeNiMnPd eutectic high-entropy alloy, *Intermetallics*, 85(2017), p. 74.

[156] S. Elkatatny, M.A.H. Gepreel, A. Hamada, K. Nakamura, K. Yamanaka, and A. Chiba, Effect of Al content and cold rolling on the microstructure and mechanical properties of $Al_5Cr_{12}Fe_{35}Mn_{28}Ni_{20}$ high-entropy alloy, *Mater. Sci. Eng. A*, 759(2019), p. 380.

[157] D. Dou, X.C. Li, Z.Y. Zheng, and J.C. Li, Coatings of FeAlCoCuNiV high entropy alloy, *Surf. Eng.*, 32(2016), No. 10, p. 766.

[158] L.H. Tian, W. Xiong, C. Liu, S. Lu, and M. Fu, Microstructure and wear behavior of atmospheric plasma-sprayed AlCoCrFeNiTi high-entropy alloy coating, *J. Mater. Eng. Perform.*, 25(2016), No. 12, p. 5513.

[159] S.Z. Niu, H.C. Kou, J. Wang, and J.S. Li, Improved tensile properties of $Al_{0.5}CoCrFeNi$ high-entropy alloy by tailoring microstructures, *Rare Met.*, 40(2021), No. 9, p. 1.

[160] M.L. Wang, G.J. Zhang, H.Z. Cui, Y.P. Lu, Y. Zhao, N. Wei, and T.J. Li, Effect of plasma remelting on microstructure and properties of a $CoCrCuNiAl_{0.5}$ high-entropy alloy prepared by spark plasma sintering, *J. Mater. Sci.*, 56(2021), No. 9, p. 5878.

[161] Y. Dong, Y.P. Lu, J.R. Kong, J.J. Zhang, and T.J. Li, Microstructure and mechanical properties of multi-component AlCrFeNiMo$_x$ high-entropy alloys, *J. Alloys Compd.*, 573(2013), p. 96.

[162] L.R. Shaginyan, V.F. Gorban', N.A. Krapivka, S.A. Firstov, and I.F. Kopylov, Properties of coatings of the Al–Cr–Fe–Co–Ni–Cu–V high entropy alloy produced by the magnetron sputtering, *J. Superhard Mater.*, 38(2016), No. 1, p. 25.

[163] P.K. Huang, J.W. Yeh, T.T. Shun, and S.K. Chen, Multi-principal-element alloys with improved oxidation and wear resistance for thermal spray coating, *Adv. Eng. Mater.*, 6(2004), No. 1-2, p. 74.

[164] M. Zhu, L.J. Yao, Y.Q. Liu, M. Zhang, K. Li, and Z.Y. Jian, Microstructure evolution and mechanical properties of a novel CrNbTiZrAlx ($0.25 \leq x \leq 1.25$) eutectic refractory high-entropy alloy, *Mater. Lett.*, 272(2020), art. No. 127869.

[165] C.D. Dai, Y. Fu, J.X. Guo, and C.W. Du, Effects of substrate temperature and deposition time on the morphology and corrosion resistance of $FeCoCrNiMo_{0.3}$ high-entropy alloy coating fabricated by magnetron sputtering, *Int. J. Miner. Metall. Mater.*, 27(2020), No. 10, p. 1388.

[166] Y. Dong, K.Y. Zhou, Y.P. Lu, X.X. Gao, T.M. Wang, and T.J. Li, Effect of vanadium addition on the microstructure and properties of AlCoCrFeNi high entropy alloy, *Mater. Des.*, 57(2014), p. 67.

[167] Z.N. An, H.L. Jia, Y.Y. Wu, P.D. Rack, A.D. Patchen, Y.Z. Liu, Y. Ren, N. Li, and P.K. Liaw, Solid-solution CrCoCuFeNi high-entropy alloy thin films synthesized by sputter deposition, *Mater. Res. Lett.*, 3(2015), No. 4, p. 203.

[168] R. Bureš, H. Hadraba, M. Fáberová, P. Kollár, J. Füzer, P. Roupcová, and M. Strečková, FeSiBAlNiMo high entropy alloy prepared by mechanical alloying, *Acta Phys. Pol. A*, 131(2017), No. 4, p. 771.

[169] J.J. Yi, L. Wang, L. Zeng, M.Q. Xu, L. Yang, and S. Tang, Excellent strength-ductility synergy in a novel single-phase equiatomic CoFeNiTiV high entropy alloy, *Int. J. Refract. Met. Hard Mater.*, 95(2021), art. No. 105416.